

IMPACT OF ROTATION ON MAGNETIC FIELD STABILITY AND ORIENTATION IN ISOLATED NEUTRON STARS

FABRIZIO VENTURI PIÑAS¹, ANSON KA LONG YIP², PATRICK CHI-KIT CHEONG^{3,4,5}, MILTON RUIZ¹

¹Departamento de Astronomía y Astrofísica, Universitat de València, Dr. Moliner 50, 46100, Burjassot (València), Spain

²Department of Physics, The Chinese University of Hong Kong, Shatin, N.T., Hong Kong

³Department of Physics, University of California, Berkeley, Berkeley, CA 94720, USA

⁴Center for Nonlinear Studies, Los Alamos National Laboratory, Los Alamos, NM 87545, USA

⁵Department of Physics & Astronomy, University of New Hampshire, 9 Library Way, Durham NH 03824, USA

Draft version August 29, 2025

ABSTRACT

Neutron stars are the most compact horizonless objects in the Universe, exhibiting the strongest known magnetic fields. They are potential sources of coincident gravitational waves and electromagnetic radiation across the entire spectrum. However, the internal configuration of their magnetic fields and the mechanisms that stabilize them remain open questions. As a step forward in understanding the timescale for the emergence of magnetic instabilities that disrupt stellar field configurations, we study the impact of stellar rotation using three-dimensional general relativistic numerical simulations of uniformly rotating, isolated neutron stars threaded by strong, poloidal, pulsar-like magnetic fields. The initial stellar configurations assume perfect conductivity and are stationary and axisymmetric. We explore a range of angular velocities, from non-rotating stars to those near the mass-shedding limit. We find that the stars spontaneously develop differential rotation, which triggers the appearance of a strong toroidal magnetic field component. Non-rotating neutron stars are unstable to the Tayler and Parker instabilities, which significantly change the magnetic field geometry. These instabilities lead to a rapid reduction of the initial magnetic energy by $\sim 99\%$ within ~ 4 Alfvén times of their onset. In contrast, rotation significantly delays the development of these instabilities and, in some cases, mitigates their effects. Highly rotating models retain up to $\sim 30\%$ of their magnetic energy for at least ~ 10 Alfvén times. Our results suggest that rotation plays a crucial role in stabilizing the magnetic field of neutron stars, regardless of its initial configuration.

Subject headings: stars: neutron –stars: magnetic field –stars: magnetars – (stars:) pulsars: general–gravitation—gravitational waves

1. INTRODUCTION

Neutron stars (NSs) are formed from the remnants of massive stars that have undergone supernova explosions (Woosley et al. 2002; Lattimer & Prakash 2001; Bethe & Brown 1995). These stars exhibit extraordinarily strong magnetic fields and can be classified into several categories: i) old-recycled pulsars with surface magnetic fields around 10^8 G (Camilo et al. 1994; Konar & Bhattacharya 1997); ii) typical pulsars with fields around 10^{12} G (Konar & Bhattacharya 1997; Bhattacharya & Srinivasan 1991); and iii) magnetars, with fields reaching up to or exceeding 10^{15} G (Duncan & Thompson 1992; Thompson & Duncan 1993, 1996). There are at least two leading hypotheses to explain the formation of such powerful magnetic fields: i) the fossil field origin, where the magnetic field is inherited from the progenitor star (Ferrario & Wickramasinghe 2006; Spruit 2008; Braithwaite & Spruit 2004); and ii) a dynamo mechanism operating during the proto-neutron star stage (Thompson & Duncan 1996; Reisenegger 2003; Brandenburg & Subramanian 2005). While modest growth of the magnetic field can also occur due to thermoelectric effects (Viganò et al. 2021; Thompson & Duncan 1996), these processes are unlikely to generate the extreme magnetar-scale fields.

These strong magnetic fields play a key role in the observable phenomena of NSs, such as the magnetic dipole radiation

seen in pulsars and the magnetically-powered burst activity of magnetars (Goldreich & Julian 1969; Thompson & Duncan 1995). They are typically invoked to explain the quasi-periodic oscillations detected following magnetar giant flares (see e.g. Gabler et al. (2011); Sotani et al. (2007)). Additionally, magnetic fields may induce deformations that could lead to significant gravitational wave emissions and precession (Bonazzola & Gourgoulhon 1996; Cutler 2002; Wasserman 2003). They also influence the thermal evolution of the star (Viganò et al. 2021; Thompson & Duncan 1996), among other effects.

The fate of NSs and possible gravitational and electromagnetic (EM) signals are therefore influenced by their internal magnetic field configuration, though its geometry remains largely uncertain. Observations of pulsar spinning down suggest that the external magnetic field is predominantly poloidal and dipolar, a configuration that aligns with the lighthouse-like radiation pattern typical of radio pulsars. However, this focus on the dipolar component is a strong simplification (Ascenzi et al. 2024), as various internal magnetic field configurations could produce a similar external appearance (Braithwaite & Spruit 2006a; Braithwaite 2009a), potentially masking the true complexity of the stellar interior.

The challenge of probing the internal magnetic field geometry has driven significant efforts into equilibrium models of magnetized NSs. Early models focused on simple mag-

netic configurations, such as purely poloidal or purely toroidal fields (Prendergast 1956; Tayler 1973; Kiuchi et al. 2008a; Lander 2013). Though in recent years, numerical studies have increasingly explored more complex mixed poloidal-toroidal fields, motivated by the need to more accurately represent the conditions within NSs (see e.g. Cioffi et al. (2009a); Pili et al. (2014); Glampedakis & Lasky (2015); Tsokaros et al. (2022); Cheong et al. (2025) and references therein). An open question still remains regarding the long-term stability of magnetic fields, as they must endure for timescales far exceeding the dynamical ones. It is well known that purely poloidal or purely toroidal magnetic field configurations can indeed be equilibrium solutions. However, such configurations tend to be dynamically unstable. Purely poloidal fields tend to become unstable due to the so-called pinch instability (Kruskal & Schwarzschild 1954; Wright 1973; Spruit 1999; Braithwaite & Spruit 2006a), while toroidal fields are prone to the so-called Tayler instabilities (Tayler 1973), and of particular importance the kink instability (Begelman 1998; Lander & Jones 2009; Braithwaite 2009a). These instabilities may also be triggered in more general magnetic field configurations. The timescale for the growth of these instabilities is typically on the order of the Alfvén timescale

$$\tau_A \sim 10 \text{ ms} \left(\frac{R_{\text{NS}}}{10 \text{ km}} \right) \left(\frac{B}{10^{15} \text{ G}} \right)^{-1} \left(\frac{\rho}{10^{14} \text{ g cm}^{-3}} \right)^{1/2}, \quad (1)$$

R_{NS} is the typical length scale of the system (radius of the NS), B is the magnetic field strength, and ρ is the rest-mass density. It is worth mentioning that usually the so-called Flowers-Ruderman mechanism (Flowers & Ruderman 1977), an oversimplified toy model, is invoked to explain the instability of the poloidal magnetic fields. It uses the analogy of two bar magnets trying to align. Magnetic field lines can realign to lower the system’s energy, driving an instability. This process is influenced by the stellar rotation, with different timescales depending on the relation between the star rotation period T_r and the Alfvén time τ_A . For $T_r \gg \tau_A$, the instability timescale is approximately τ_A , while for $T_r \ll \tau_A$, it becomes $\tau_{\text{MHD}} \approx 2\tau_A^2/T_r$, the timescale for the magnetic field to realign through internal fluid motions in a rotating, conductive fluid.

Recently magnetohydrodynamic (MHD) studies (see e.g. Braithwaite & Nordlund (2005); Cioffi et al. (2009b); Lander & Jones (2009); Cioffi et al. (2010); Gabler et al. (2013); Tsokaros et al. (2022); Cheong et al. (2025) and references therein) have suggested that NS magnetic fields are much more complex. These fields are likely a mixture of poloidal and toroidal components, which interact in intricate ways that were not fully captured by this mechanism. Mixed poloidal-toroidal configurations are often considered more stable and realistic for modeling the magnetic fields of NSs (Braithwaite & Nordlund 2005; Cioffi et al. 2009b; Lander & Jones 2009; Cioffi et al. 2010; Gabler et al. 2013; Tsokaros et al. 2022; Cheong et al. 2025). The superposition of poloidal and toroidal magnetic field components may lead to a more stable configuration than configurations with only one component, as they can potentially counterbalance each other’s instabilities. However, the overall stability depends on the specific configuration and the relative strengths of the poloidal and toroidal components. Numerical simulations in both Newtonian and general relativistic frameworks have shown that these configurations can remain stable over significant timescales, though they may eventually succumb

to instabilities, such as varicose or kink instabilities (see e.g. Tsokaros et al. (2022)). The latter instability is triggered when the toroidal magnetic field becomes too strong relative to the stabilizing forces, leading to displacements in the plasma perpendicular to the field lines (Lander & Jones 2011; Markey & Tayler 1973; Braithwaite 2009a).

Over the past two decades, studies on the stability of the magnetic field of NS have increasingly focused on the field geometry, i.e. the distribution of the poloidal and toroidal components, rather than physical mechanisms that affect its evolution. In this work, we probe how the angular velocity of the NS affects the evolution of the magnetic field. In pursuit of this goal, we perform general relativistic magnetohydrodynamic (GRMHD) simulations of rapidly rotating, self-consistent magnetized NSs with a pulsar-like magnetic field extending from the stellar interior into the exterior. The stars that are initially uniformly rotating with angular velocities ranging from non-rotation to half the mass-shedding limit. The maximum magnetic field strength in our configuration reaches $\sim 10^{17}$ G. We note that astronomical observations primarily constrain the magnetic field strength at the surface of the NS (particularly at the poles) rather than the strength within the NS, which can be significantly higher. The virial theorem provides an upper limit, suggesting that the internal magnetic field strength could reach up to $\sim 10^{18}$ G (Goldreich & Julian 1969; Reisenegger 2013). Although this field strength is significantly larger from an astronomical perspective, it is dynamically weak, with a magnetic-to-gas-pressure ratio $\beta^{-1} = P_{\text{mag}}/P \ll 1$. This ensures that we can effectively capture magnetic instabilities within the constraints of our computational resources.

We find that rotation can suppress or at least delay the onset of various magnetic instabilities for at least 10 Alfvén times. Unlike cases with low rotation, where the system loses about 99% of its initial magnetic energy in only 4 Alfvén times from the onset of the instability, highly rotating cases retain up to 30% of their magnetic energy. Our results suggest that rotation may be crucial in stabilizing the magnetic field of NSs, regardless of its initial configuration. We also observe that the star spontaneously develops differential rotation within its core followed by a magnetic field misalignment with respect to the angular velocity.

The remainder of the paper is organized as follows. In Sec. 2.1 we briefly review our numerical methods and their implementation, referring the reader to (Cordero-Carrión et al. 2009; Bucciantini & Del Zanna 2011; Pili et al. 2017, 2014, 2015; Cheong et al. 2021b) for further details and code tests. A detailed description of the adopted initial data and the grid structure employed for the evolution is given in Secs. 2.2 and 2.3. A suite of diagnostics used to verify the reliability of our numerical calculations are summarized in Sec. 2.4. In Sec. 3, we review the magnetic instabilities our configurations may be unstable to. We present our results in Sec. 4 and summarize our results and conclude in Sec. 5. Additionally, in Appendices A and B we probe the impact of the variable atmosphere present in our simulations and the impact of the resolution in our results. Throughout the paper we adopt Heaviside-Lorentz units, for which the speed of light c , gravitational constant G , solar mass M_\odot , vacuum permittivity ϵ_0 , are set to one ($c = G = M_\odot = \epsilon_0 = 1$).

2. NUMERICAL METHODS

2.1. Simulation setup

The numerical methods used in this study have been thoroughly detailed in previous works (see, e.g., [Cheong et al. \(2020, 2021b, 2022, 2023\)](#)). Here, we provide only a brief overview of the key aspects, directing the reader to those references for a detailed discussion and code validation.

We perform full 3D ideal GRMHD simulations using the well-tested `Gmunu` code. The code solves the Einstein equations using the approximation so-called extended conformal flatness condition (xCFC) ([Cordero-Carrión et al. 2009](#)), which equations are elliptical in nature, using a non-linear cell-centred multi-grid approach (see Eqs. (72)–(76) in [Cheong et al. \(2021b\)](#)). The matter and magnetic fields are evolved using the equations of ideal GRMHD, which are cast in a conservative scheme (see Eqs. (25)–(28) in [Cheong et al. \(2021b\)](#)), via a high-resolution shock capturing technique employing the 3rd-order reconstruction piecewise parabolic method ([Colella & Woodward 1984](#)) coupled to the Harten, Lax, and van Leer approximate Riemann solver ([Harten et al. 1983](#)). For time integration, strong-stability preserving Runge–Kutta of third order (SSPRK3) ([Shu & Osher 1988](#)) is used with a Courant–Friedrichs–Lewy (CFL) factor set to 0.25. To ensure the magnetic field remains divergenceless during the whole evolution, we integrate the magnetic induction equation using the so-called staggered-meshed constrained transport ([Evans & Hawley 1988](#)). `Gmunu` uses adaptive mesh refinement (AMR) to resolve different scales accurately when needed. The parallelization and AMR of `Gmunu` is provided by the coupling `MPI-AMRVAC` toolkit ([Xia et al. 2018; Keppens et al. 2020; Keppens et al. 2023](#)), which is an open-source message passing interface (MPI) based parallelized toolkit with a pure block-tree AMR module.

Empirical results from [Bucciantini & Del Zanna \(2011\); Cheong et al. \(2021b\)](#) suggest that solving the xCFC equations every 10 to 50 time steps provides an acceptable balance between accuracy and efficiency for isolated NS simulations. In the simulations reported here, we choose to solve the xCFC equations every 10 time steps to maintain consistency with these findings. Finally, we adopt a Γ –law equation of state (EoS) $P = (\Gamma - 1)\rho\epsilon$, allowing for shock heating. Here, ϵ is the specific internal energy and P is the pressure. We set $\Gamma = 2$, which reduces to a polytropic law for the initial (cold) NS matter (see below).

2.2. Initial data

We consider equilibrium configurations of uniformly rotating and magnetized NS, spanning from non-rotating to those approaching half the mass-shedding limit. As our goal is to probe the effects of the angular velocity on the emergence of magnetic instabilities, we model the stars with a simple polytropic EoS $P = K\rho_0^\Gamma$. The polytropic constant K is set to 218.23 km^2 , what induces a Tolman–Oppenheimer–Volkoff (TOV) maximum mass of $\sim 1.64 M_\odot$.

The initial data (ID) of the axisymmetric equilibrium configurations are computed using the open source code `Xtended Numerical Solver (XNS)` ([Bucciantini & Del Zanna 2011; Pili et al. 2017, 2014, 2015](#)). These models have a purely poloidal magnetic field defined through the magnetization function (see Eq. (32) in [Pili et al. \(2014\)](#))

$$\mathcal{M}(A_\phi) = k_{\text{pol}} \left(A_\phi + \xi \frac{1}{2} A_\phi \right), \quad (2)$$

which defines the distribution of the magnetic field (see left column in Fig. 1). Here, A_ϕ is the vector potential, k_{pol} is

the poloidal magnetization constant that controls the strength of the magnetic field, and ξ is the non-linear poloidal term. We choose k_{pol} such that the maximum value of the magnetic field $B_{\text{max}} \approx 1.5 \times 10^{17} \text{ G}$ for all models listed in Table 1. While the resulting magnetic field strength is large from an astrophysical point of view, it is dynamically weak (i.e. $\beta^{-1} \ll 1$) and enables us to resolve the magnetic instabilities with the finite computational resources at our disposal.¹ We note that such strong magnetic fields appear in magnetar scenarios (i.e. NSs with extremely strong magnetic fields $\gtrsim 10^{15} \text{ G}$) have been suggested as a likely source of Soft Gamma repeaters and Anomalous X-ray Pulsars ([Thompson & Duncan 1996; Mereghetti 2008](#)). In addition, during and immediately following core collapse and the formation of a proto-neutron star, the immense reservoir of free energy can drive the amplification of magnetic fields to extreme strengths, potentially reaching up to $\sim 10^{17} - 10^{18} \text{ G}$ ([Burrows et al. 2007; Rembiasz et al. 2016](#)).

We consider a set of five magnetized NS models, a non-rotating reference model named P1U0 (i.e. poloidal-uniform-number-case) and four rotating models (see Table 1). In all models we set the central rest-mass density of $\rho_c \sim 7.9 \times 10^{14} \text{ g cm}^{-3}$. The angular velocity ranges from slow rotation (P1U1 case) to half the mass-shedding limit (P1U4 case).

Following [Ruiz et al. \(2018\); Paschalidis et al. \(2015\)](#), at the beginning of the simulations, we impose a low-density, variable magnetosphere with a magnetic-to-gas pressure ratio of $\beta^{-1} \leq 10^{-3}$ in the exterior of the star. This method has been successfully employed in previous studies (see e.g. [Ruiz et al. \(2021a\)](#)) to reliably evolve magnetic fields in environments dominated by magnetic pressure. Following [Cheong et al. \(2025\)](#), we consider that any point at which the rest-mass density ρ falls below the threshold ρ_{thr} is part of the atmosphere. This threshold is set to be eleven orders of magnitude smaller than the initial maximum density, i.e. we set $\rho_{\text{thr}} = 10^{-11} \rho_{\text{max}}(t = 0) \sim 4 \times 10^{-14}$. For points falling below this threshold, the rest mass density is reset to $\rho_{\text{atm}} = 0.9\rho_{\text{thr}}$. Through empirical numerical experiments, we find that the non-rotating, slow and middle rotation models are stable with a magnetic-to-gas-pressure ratio of $\beta^{-1} = 10^{-6}$. However, higher rotation modes require a heavier atmosphere likely due to larger magnetic gradients induced by rotation. For these cases, we find that the magnetic-to-gas pressure ratio should be $\beta^{-1} = 10^{-4}, 10^{-3}$ for P1U3 and P1U4, respectively. To assess the robustness of the numerical evolution of the magnetized NS against the effects of the artificial atmosphere treatment, we evolve model P1U2 using the three setups described above (see Appendix A). We find that this treatment has a minimal impact on the final outcome of the magnetic field configuration, and so on the magnetic energy.

2.3. Grid structure

All NS configurations in Table 1 are evolved using Cartesian coordinates (x, y, z) without imposing any symmetries to prevent the suppression of some instabilities. The computational domain spans $[-180 \text{ km}, 180 \text{ km}]$ along each direction with a resolution of $N_x \times N_y \times N_z = 128^3$ grid points, and using four AMR levels differing in size and resolution by a factor of two. The outer boundary is located at $\sim 15 R_e$,

¹ The stronger the magnetic field, the shorter the growth timescale τ_A of the instabilities.

TABLE 1

SUMMARY OF THE INITIAL PROPERTIES OF THE MAGNETIZED NS CONFIGURATIONS. WE LIST THE NAME OF THE CONFIGURATION P1UX (POLOIDAL-UNIFORM-NUMBER-CASE), THE BARYONIC MASS M_0 , THE ROTATIONAL PERIOD T_r (RANGING FROM ZERO TO HALF OF THE MASS-SHEDDING LIMIT), THE COORDINATE EQUATORIAL RADIUS R_e , THE POLAR-TO-EQUATORIAL-RADIUS RATIO R_p/R_e , THE TOTAL MAGNETIC ENERGY, THE MAGNETIC-TO-BINDING-ENERGY RATIO E_B/\mathcal{W} , AND THE KINETIC-TO-BINDING-ENERGY RATIO E_K/\mathcal{W} . IN ALL OF THESE MODELS, THE CENTRAL REST-MASS DENSITY IS FIXED TO $\rho_c \simeq 7.9 \times 10^{14} \text{ g cm}^{-3}$.

Case	$M_0 [M_\odot]$	$T_r [\text{ms}]$	$R_e [\text{km}]$	R_p/R_e	$E_{B_{\text{tot}}} [\text{erg}]$	$E_{B_{\text{tot}}}/\mathcal{W}$	E_K/\mathcal{W}
P1U0	1.51	∞	12.01	0.98	1.50×10^{51}	4.26×10^{-3}	0.0
P1U1	1.52	6.19	12.01	0.98	1.55×10^{51}	0.33	3.16×10^{-3}
P1U2	1.54	3.09	12.22	0.94	1.65×10^{51}	0.33	1.29×10^{-2}
P1U3	1.59	2.06	12.56	0.89	1.66×10^{51}	0.32	2.95×10^{-2}
P1U4	1.66	1.55	13.26	0.81	1.82×10^{51}	0.30	5.49×10^{-2}

where R_e is the coordinate equatorial stellar radius (see Table 1). The highest-resolution grid covering the NS has a spatial resolution of $\Delta x = \Delta y = \Delta z \approx 345 \text{ m}$. To probe the impact of the numerical resolution on our results (see Appendix B), we run the P1U2 model at two additional resolutions: a “medium” resolution (MR), in which the finest refinement level has grid spacing of $\Delta x = \Delta y = \Delta z \approx 230 \text{ m}$, and a “high” resolution (HR), in which the finest level has spacing $\Delta x = \Delta y = \Delta z \approx 173 \text{ m}$. Refinements are fixed after initialization, as a significant star expansion is not observed.

2.4. Diagnostics

To verify the reliability of our simulations, we monitor the conservation of the total mass M_{int} (see e.g. Eqs. (3.128) and (3.191)) in (Baumgarte & Shapiro 2010), which coincides with the ADM mass M_{ADM} when evaluated at spatial infinity, as well as the conservation of the rest-mass M_{rest} (see e.g. Eq. (3.127) in (Baumgarte & Shapiro 2010), and the proper mass M_{proper} computed in the case of the xCFC spacetime as

$$M_{\text{ADM}} = \int \left(\rho_H + \frac{K^{ij} K_{ij}}{16\pi} \right) \psi^5 dx^3, \quad (3)$$

$$M_{\text{rest}} = \int \rho W \psi^6 dx^3, \quad (4)$$

$$M_{\text{proper}} = \int \rho W (1 + \varepsilon) \psi^6 dx^3, \quad (5)$$

with W the Lorentz factor, ε the fluid specific internal energy, ψ the conformal factor, K^{ij} is the extrinsic curvature, and

$$\rho_H = T_{\alpha\beta} n^\alpha n^\beta = \rho h W^2 - P + \frac{1}{2} (E^2 + B^2). \quad (6)$$

We note that the total stress-energy tensor $T_{\alpha\beta}$ is the sum of the stress-energy tensor for a perfect fluid and the stress-energy tensor for the electromagnetic field, n^α is the normal to the hypersurface, $P = P_{\text{gas}}$ is the pressure of the fluid, $E^2 = E^i E_i$, $B^2 = B^i B_i$, and E^i , B^i are the purely spatial electric, magnetic fields with respect to the normal observer, and $h = 1 + \varepsilon + P/\rho$ is the specific enthalpy.

Consistent with Cheong et al. (2021a), we find that in all cases listed in Table 1 the above masses and the ADM angular momentum are conserved to within $\lesssim 1.6\%$ throughout the entire evolution (Cordero-Carrión et al. 2009). We calculate the internal energy, the kinetic energy, the pressure con-

tribution, and the electromagnetic energy defined as

$$E_{\text{int}} = \int \epsilon_{\text{int}} \psi^6 dx^3, \quad (7)$$

$$E_{\text{kin}} = \int \epsilon_{\text{kin}} \psi^6 dx^3, \quad (8)$$

$$E_{\text{prs}} = \int \epsilon_{\text{prs}} \psi^6 dx^3, \quad (9)$$

$$E_{\text{EM}} = \int \epsilon_{\text{EM}} \psi^6 dx^3, \quad (10)$$

where,

$$\epsilon_{\text{int}} = \rho W^2 \varepsilon, \quad (11)$$

$$\epsilon_{\text{kin}} = \rho W (W - 1), \quad (12)$$

$$\epsilon_{\text{prs}} = P (W^2 - 1), \quad (13)$$

$$\epsilon_{\text{EM}} = \frac{1}{2} (B^2 + E^2). \quad (14)$$

The total energy can be calculated either by adding the individual components $E_{\text{tot}} = E_{\text{int}} + E_{\text{kin}} + E_{\text{prs}} + E_{\text{EM}}$ or by integrating the total conserved energy density over the entire volume as

$$E_{\text{tot}} = \int \mathcal{E}_{\text{tot}} \psi^6 dx^3, \quad (15)$$

with

$$\mathcal{E}_{\text{tot}} = \rho h W^2 - P + \frac{1}{2} (E^2 + B^2) - \rho W. \quad (16)$$

The characteristic timescale for magnetic field evolution is the Alfvén time,

$$\tau_A = \frac{2 R_{\text{NS}} \sqrt{\rho_{\text{avg}}}}{B_{\text{avg}}}, \quad (17)$$

where ρ_{avg} and B_{avg} are the average rest-mass density and magnetic field strength computed within the bulk of the NS. Since these averages evolve over time, the Alfvén time is a dynamic quantity that changes throughout the evolution. Fig. 2 shows the evolution of τ_A as a function of the coordinate time for the cases in Table 1. We note that τ_A increases only after the onset of magnetic instabilities (see below). Following this, and depending on the initial angular velocity of the NS, the Alfvén time either increases linearly with coordinate time, or reaches a plateau where it grows more slowly. To account for this time dependence, following (Sur et al. 2022), we define the Alfvén crossing time as

$$T_A = \int_0^t \frac{1}{\tau_A(t)} dt. \quad (18)$$

TABLE 2
EVOLUTION TIMES FOR ALL NS CASES LISTED IN TABLE 1. WE LIST THE TIME IN UNITS OF MILLISECONDS AND ALFVÉN CROSSING TIME T_A .

Model	Time [ms]	Time [T_A]
P1U0	103.70	9.44
P1U1	133.00	9.58
P1U2	103.80	10.16
P1U3	100.30	13.18
P1U4	88.20	13.04

We rescale the evolution time using the Alfvén crossing period T_A and hence a value of $T_A = n$ indicates that the system has evolved for a time equivalent to $n \tau_A$. We note that T_A varies across different cases due to changes in the magnetic energy and the evolving density over time. During the beginning of the simulation, advancing by one τ_A corresponds roughly to 4 ms of physical time across all models. However, by the end of the simulations, a τ_A corresponds to ~ 55 ms for model P1U0 and ~ 20 ms for P1U2. This difference arises because the average magnetic field strength B_{avg} decays more rapidly in P1U0 compared to the other models, as shown in Fig. 3. Table 2 shows the evolution time in units of milliseconds and its corresponding Alfvén crossing time.

On the other hand, we define the poloidal and toroidal magnetic field components splitting B^i into

$$B^i \equiv B_{\text{tor}} \hat{e}_{\text{tor}}^i + B_{\text{pol}} \hat{e}_{\text{pol}}^i, \quad (19)$$

where \hat{e}_{tor}^i , \hat{e}_{pol}^i are orthonormal 3-vectors such that $q_{ij} \hat{e}_{\text{tor}}^i \hat{e}_{\text{tor}}^j = q_{ij} \hat{e}_{\text{pol}}^i \hat{e}_{\text{pol}}^j = 1$, $q_{ij} \hat{e}_{\text{tor}}^i \hat{e}_{\text{pol}}^j = 0$ and $\hat{e}_{\text{tor}}^i \propto (-y, x, 0)$ in Cartesian coordinates. Here q_{ij} is defined as (Bamber et al. 2025)

$$q_{ij} = \gamma_{ij} (1 + w_k w^k) - w_i w_j, \quad (20)$$

$$w^i = (v^i + \beta^i) / \alpha, \quad (21)$$

with v^i the three velocity, and α and β^i the lapse and the shift vector, respectively. We also define the magnetic field strength

$$B = \psi^2 \sqrt{\delta_{ij} B^i B^j}, \quad (22)$$

with $\delta_{ij} = \text{diag}(1, 1, 1)$.

In addition, we monitor the total magnetic field energy

$$E_{\text{Btot}} = \frac{1}{2} \int B^i B_i \psi^6 dx^3, \quad (23)$$

the toroidal magnetic energy,

$$E_{\text{Btor}} = \frac{1}{2} \int (B_{\text{tor}})^i (B_{\text{tor}})_i \psi^6 dx^3, \quad (24)$$

and the poloidal magnetic energy,

$$E_{\text{Bpol}} = E_{\text{Btot}} - E_{\text{Btor}}, \quad (25)$$

to study how the toroidal and poloidal magnetic energy develops during the evolution. As the system evolves, the magnitude and the geometry of the initial poloidal magnetic field are expected to change due to the instabilities (see Sec. 3) in a timescale of the order of an Alfvén time, what has been confirmed by previous numerical studies (see e.g. Braithwaite, J. (2007); Sur et al. (2022); Tsokaros et al. (2022)). We note that the initial value of the Alfvén time is ~ 4 ms for all models.

It is worth noting that rotation may change the timescale of certain instabilities. Pitts & Tayler (1985) showed that in rapidly rotating models, magnetic instabilities appear roughly at around τ_A^2 / T_r , where T_r is the stellar rotational period (see also Spruit (2008) and Flowers & Ruderman (1977)). Therefore, in our fastest rotating model (P1U4), we will expect the instabilities to be triggered at ~ 10 ms.

3. INSTABILITIES IN MAGNETIC FIELDS AND THE ROLE OF ROTATION

As discussed in Sec. 1, magnetized NSs are prone to various magnetic instabilities that can considerably influence the evolution of their magnetic fields, potentially causing magnetic field reconfigurations and releasing energy in the form of heat, EM radiation, or even particle acceleration. These instabilities may contribute to the gradual decay of the magnetic field. In the following, we review some of the most significant of these instabilities:

1. **Taylor instability:** The instability occurs in systems where the magnetic field has a strong azimuthal (toroidal) component, commonly found in cylindrical or toroidal geometries. This instability is triggered when the magnetic energy stored in the azimuthal field becomes strong enough to destabilize the system, overcoming the stabilizing effects of fluid pressure and the tension in the magnetic field lines (Taylor 1973). It typically develops on the order of the Alfvén timescale τ_A . While our configurations initially have only a poloidal magnetic field component, a strong toroidal component emerges after a few dynamical timescales (see below). Two important modes of this instability are the so-called “varicose” (or “sausage”) and the “kink”. These are characteristic deformations of the flux tubes. The former is related to radial contractions of the flux tubes, while the latter is associated with their twisting.
2. **Pinch instability:** The instability is driven by an axial current, and typically appears in poloidal magnetic field configurations, which creates a circular magnetic field around the current. The magnetic pressure generated by the current flowing through the plasma is strong enough to compress the plasma inward. If the inward magnetic pressure exceeds the outward pressure forces (thermal pressure and magnetic tension), the plasma becomes unstable, leading to collapse or constriction of the plasma column (Wright 1973; Taylor 1986). The timescale for the pinch instability is also on the order of the Alfvén timescale, similar to the Taylor instability. Also, like the Taylor instability, the pinch instability exhibits analogous varicose and kink modes.
3. **Parker or magnetic buoyancy instability:** It occurs in systems where the magnetic field has a significant horizontal component, as in poloidal and mixed (poloidal + toroidal) configurations. It is typically triggered in stratified (layering) environments where there are gradients in density or pressure. This configuration is common in the crust of NSs, where the magnetic field and the stratification of matter are aligned. The instability is triggered when buoyant forces act on the magnetic field lines, causing them to rise or fall (Parker 1966; Acheson & Gibbons 1978). It appears mainly if the magnetic field strength increases in the direction of gravity, with magnetic pressure counteracting gravitational

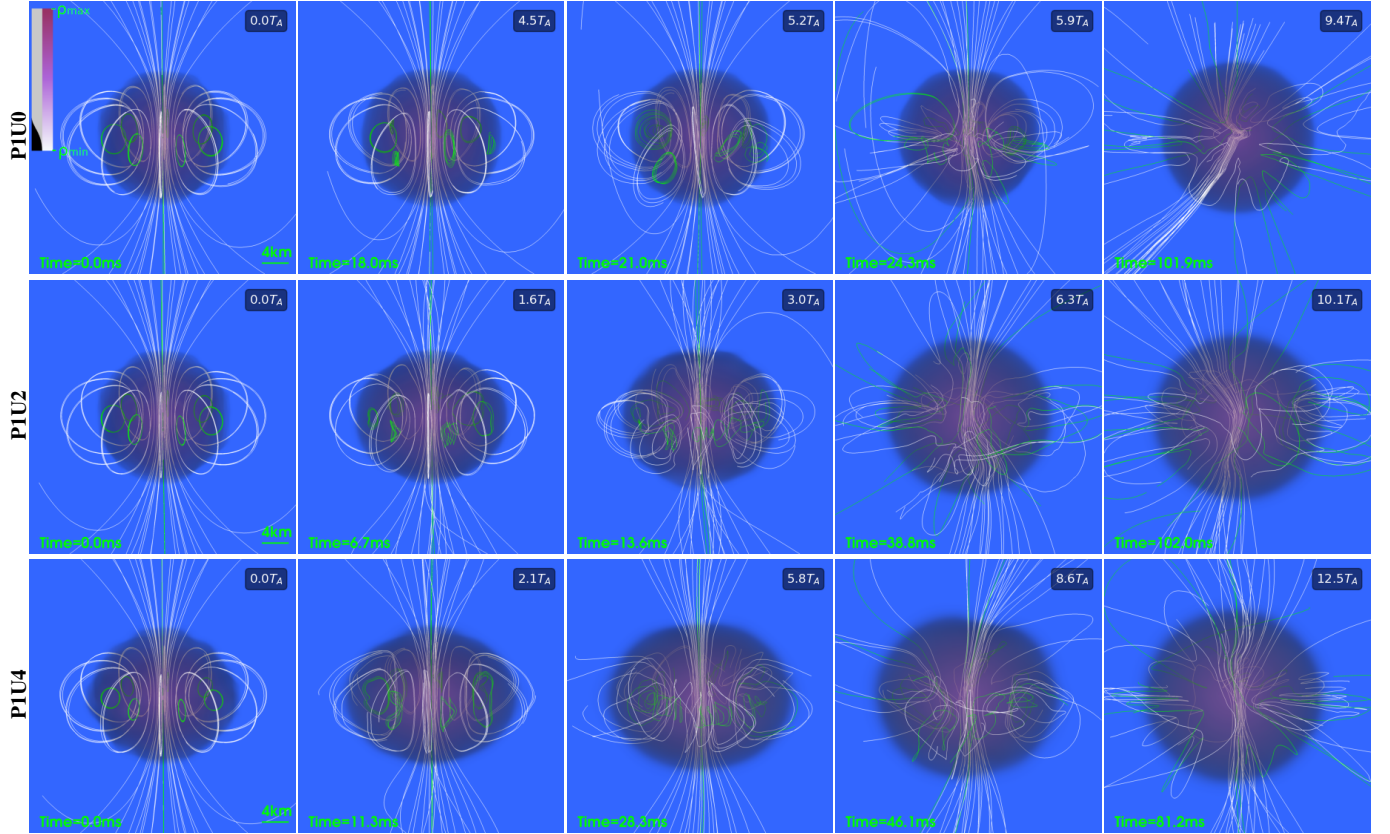


FIG. 1.— 3D volume rendering of the rest-mass density ρ at selected Alfvén crossing times for cases in Table 1 along with the magnetic field lines. Green and white lines display magnetic field lines that are either confined in the stars (green) or extend from the stellar interior into the exterior (white). The colorbar (logarithmic scale) ranges from the atmospheric density to the maximum rest-mass density at the corresponding time. The black and gray rectangles to the left of the colorbar indicate opacity, which ranges from fully opaque (black) to approximately $\sim 76\%$ opacity (gray).

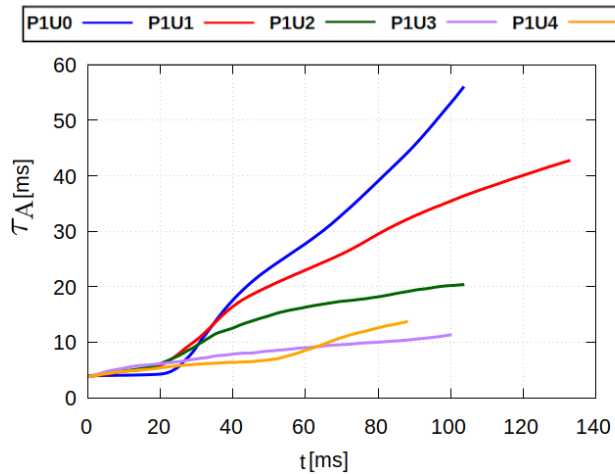


FIG. 2.— Alfvén time τ_A as defined in Eq. (17) versus the coordinate time for models in Table 1.

forces. Energy can be released as the magnetic field lines bend due to strong pressure gradients. This instability generally requires stronger magnetic fields than the Tayler instability and may play a lesser role in certain contexts. The timescale for the Parker instability is on the order of the Alfvén timescale.

The MHD simulations of NSs endowed with a purely poloidal magnetic field in (Geppert & Rheinhardt 2006) found that oblique configurations, with magnetic inclination $\lesssim 45^\circ$

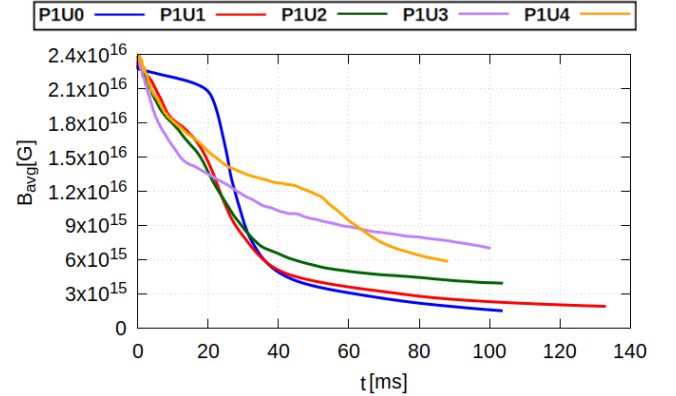


FIG. 3.— Evolution of the average magnetic field strength B_{avg} vs. the coordinate time for models listed in Table 1. The rate at which the magnetic field decays strongly depends on the initial angular velocity of the system.

could maintain high magnetic fields, while slower rotation or larger inclinations led to significant magnetic energy loss. However, the simulations in (Braithwaite & Spruit 2006b; Braithwaite, J. 2007) showed that this field configuration is unstable and decay within a few Alfvén times regardless of the angular velocity of the star, even in oblique configurations, although the rotation slows this decay. In highly rotating stars, the instability timescale is lengthened by t_A/T . Kiuchi et al. (2008b) performed axisymmetric GRMHD simulations of NSs with a pure toroidal magnetic field. They found that rapid rotation may suppress the Tayler instabil-

ity, suggesting that when kinetic energy is about six times larger than the electromagnetic energy, the magnetic field can remain stable. However, axisymmetry may artificially suppress some instabilities (see e.g. (Acheson & Gibbons 1978; Parker 1966)). Subsequent 3D simulations by Kiuchi, K. et al. (2011) of highly rotating NSs with toroidal magnetic fields suggested that magnetic instabilities, such as the Parker and Tayler instabilities, can indeed be triggered on the order of the Alfvén timescale. The GRMHD studies by Sur et al. (2022) and Tsokaros et al. (2022) found that mixed toroidal and poloidal magnetic field configurations are unstable. More recently, Cheong et al. (2025) probed the effect of resistivity on the emergence of magnetic instabilities in isolated NS endowed with both poloidal and toroidal magnetic field configurations. They found that although all configurations are unstable to the Tayler instability, resistivity can delay its growth.

4. RESULTS

The outcomes and basic dynamics for all our cases in Table 1 are similar, hence we show snapshots and discuss the evolution only for nonrotating (P1U0), middle (P1U2) and highest (P1U4) rotation cases, unless otherwise specified. We summarize key results for all cases in Table 3.

4.1. Magnetic field evolution

Fig. 1 displays the evolution of magnetic field lines for P1U0, P1U2, and P1U4 cases at different Alfvén crossing times. Note that, since these times are case-dependent (see Eq (18) and Table 3), we choose the times to highlight the onset and evolution of the magnetic instabilities for each individual case.

During the first $t \sim 3T_A$ (or ~ 10 ms), the pure poloidal magnetic field configuration of P1U0 (see top-left panel in Fig. 1) remains constant. Following this early epoch, the inner regions of the NS ($\lesssim 3$ km) spontaneously develop differential rotation with a peak value of ~ 1 kHz while the outer layers rotate roughly uniformly with $\Omega \sim 100$ Hz (see left panel in Fig. 4). We note that spontaneous differential rotation has also been observed in full GRMHD simulations of self-consistent rotating NSs seeded with poloidal and toroidal magnetic fields in (Tsokaros et al. 2022), and in resistive GRMHD simulations (Cheong et al. 2025). This effect has been attributed to the initial strong poloidal magnetic field component. The onset of differential rotation leads to the development of magnetic winding within the next $t \lesssim 1.5T_A$, and so to the emergence of a strong toroidal magnetic field component. This new magnetized NS configuration is prone to instabilities that distort the magnetic field (see top row in Fig. 1). In particular, we observe that by $t \sim 5T_A$ the poloidal field lines confined inside the NS (shown in green in the second and third panel in Fig. 1) undergo a change in their cross-sectional area, a behavior consistent with the varicose mode, which can develop due to the pinch instability (Wright 1973). This behavior has also been reported in (Sur et al. 2022). Simultaneously, and consistent with the Parker instability, weaker-tension field lines (mainly smaller loops) become buoyant due to local magnetic pressure, causing them to rise toward the lower-density regions of the star. As angular momentum is transported in the inner regions of the star, the poloidal magnetic field anchored in these regions is twisted into a toroidal configuration, causing the field lines to wind along the equatorial plane (third and fourth panels in Fig. 1). We also observe that some field lines begin to shift slightly along the magnetic axis (Braithwaite, J. 2007), a footprint

TABLE 3
SUMMARY OF THE RESULTS. WE LIST THE FRACTION OF THE INITIAL TOTAL MAGNETIC ENERGY $E_{B_{\text{tot}0}}$ REMAINING AT $T_A - T \simeq 4$ (SEE DISCUSSION IN THE MAIN TEXT) FOLLOWING THE ONSET OF THE MAGNETIC INSTABILITIES, THE TOROIDAL-TO-TOTAL MAGNETIC ENERGY RATIO AT THAT POINT, ITS MAXIMUM, AND THE AVERAGE MAGNETIC FIELD TILT ANGLE WITH RESPECT TO THE ROTATION AXIS FOR ALL NS MODELS IN TABLE 1.

Model	$E_{B_{\text{tot}}}/E_{B_{\text{tot}0}}$	$E_{B_{\text{tor}}}/E_{B_{\text{tot}}}$	$\max(E_{B_{\text{tor}}}/E_{B_{\text{tot}}})$	$\zeta_{\text{avg}} [^\circ]$
P1U0	1.13%	6.3%	10.5%	—
P1U1	7.48%	7.0%	14.7%	7.7
P1U2	16.79%	12.3%	21.4%	14.9
P1U3	59.09%	11.1%	12.8%	14.5
P1U4	19.12%	14.1%	18.5%	19.6

of the kink instability, likely associated with strong toroidal magnetic fields (Tayler 1973). By $t \sim 9T_A$, the original magnetic field configuration has been completely disrupted due to the cumulative effects of the above magnetic instabilities (see top-right panel). We note that once differential rotation is present, additional instabilities, such as the magnetorotational instability (MRI) may also operate within the star. However, given our current numerical resolution (see Sec. 2.3), it is unlikely that the inner regions of the star become unstable against the MRI (Kiuchi et al. 2024).

In the uniformly rotating cases, we observe that during the early stages of evolution, the initial poloidal magnetic field configuration remains unchanged. Subsequently, differential rotation spontaneously develops on a shorter timescale than in P1U0 (see second column in Fig. 1 and Fig. 4), around $t \sim 1.6T_A$. Differential rotation winds the poloidal magnetic field into a toroidal configuration. The varicose mode is subsequently triggered in the stars, leading to observable changes in the cross-sectional area of the interior magnetic field lines (see second column in Fig. 1). In contrast to P1U0, where the Parker instability emerges due to magnetic pressure gradients, we find no evidence of its development in these cases. It is likely that the additional centrifugal support reduces the magnetic pressure gradients within the star, thereby suppressing the Parker instability. We note that local changes in the magnetic field and enhanced magnetic tension may also contribute to stabilizing the system against magnetic buoyancy modes (Ruiz et al. 2021b; Aguilera-Miret et al. 2024). By $t \gtrsim 6.0T_A$, consistent with the onset of the kink instability, we observe slight displacements of some field lines along the magnetic axis (see the third and fourth panels in the middle and bottom rows of Fig. 1). Finally, by $t \gtrsim 10T_A$ magnetic instabilities have fully disrupted the initial magnetic field configuration (see fifth panels in the middle and bottom rows in Fig. 1). Further evidence of the kink instability can be seen through a top view of P1U4 displayed in Fig. 5. Initially, the field lines of the poloidal magnetic field (closed loops) are aligned along the rotation axis (left panel), but they become twisted at later times (right panel). A distorted quasi-axisymmetric “flower-like” structure forms as a result of the growth of the toroidal component, consistent with the development of the kink instability. Similar behavior is observed in the other rotating cases in Table 3.

4.2. Magnetic energy evolution

We now analyze the evolution of the models from an energetic point of view. We examine the total magnetic energy $E_{B_{\text{tot}}}$ as defined in Eq. (23), along with the toroidal and poloidal energies as given by Eqs. (24) and (25), respectively.

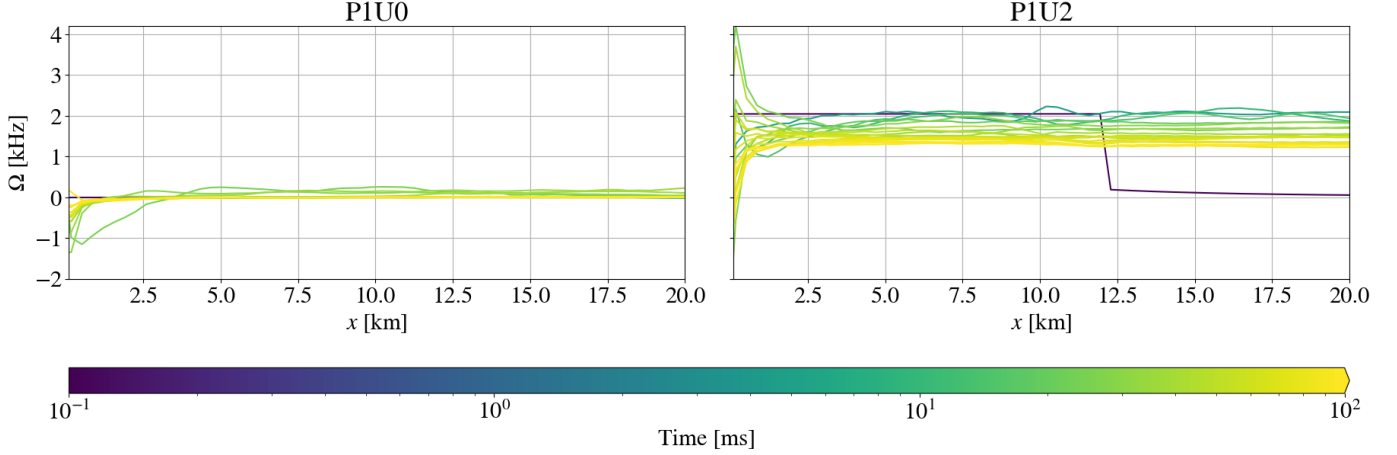


FIG. 4.— Angular velocity profiles along the coordinate x -axis for the non-rotating case P1U0 (left) and the mildly rotating case P1U2 (right). Differential rotation spontaneously develops in the cores of the stars (roughly in the region contained within $\lesssim 3$ km) regardless of their initial rotation profile. Similar behavior is observed in the other cases in Table 1.

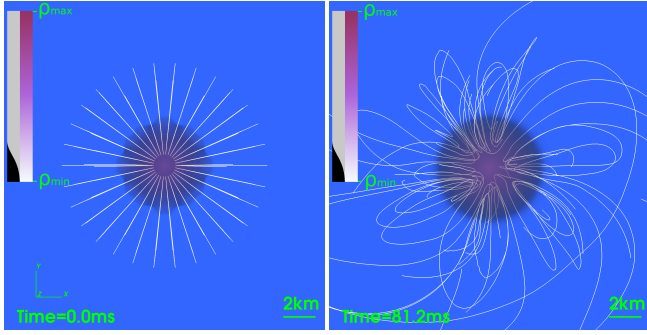


FIG. 5.— Top view of the rest-mass density of P1U4, along with the field lines at $T_A = 0$ (left) and near to the end of the simulation ($\approx 12.5 T_A$). The colorbar (logarithmic scale) ranges from the atmospheric density to the maximum rest-mass density at the corresponding time. The black and gray rectangles to the left of the colorbar indicate opacity, which ranges from fully opaque (black) to $\sim 76\%$ opacity (gray).

We focus on assessing the stability of the systems and evaluating how rotation influences the emergence of a toroidal component and how both rotation and magnetic instabilities contribute to its evolution.

The upper panel of Fig. 6 displays the total magnetic energy $E_{B_{\text{tot}}}$ vs. the Alfvén crossing time for all cases and shifted by a time T . We define T as the time at which the total magnetic energy has decreased by 10%. Therefore, negative times ($t - T < 0$) indicate how long the system remains stable before the instability sets in, while positive times ($t - T > 0$) show how long the instabilities have been operating in the system. We note that before $t \sim 5 T_A$, the Parker and varicose instabilities are operating in P1U0 (see discussion above). However, the total magnetic energy remains roughly constant during this epoch. By $t \sim 5 T_A$, the magnetic energy begins to decline, marking the onset of the kink instability. By $t \sim 6 T_A$ (or $T_A - T \sim 0.5$), the initial magnetic field configuration has been disrupted, and the magnetic energy drops sharply.

Although we evolve all cases for approximately 100 ms (see Fig. 2), the onset of magnetic instabilities limits the evolution of the P1U0 and P1U4 models to about $T_A - T \simeq 4$, which is marked as a gray line in Fig. 6. To ensure a fair comparison across all models, we restrict our analysis to this period of time and then comment on the subsequent evolution for models that extend beyond this time.

We note that the slope decay of $E_{B_{\text{tot}}}$ depends on the angular velocity. In general, the slower the star rotates, the steeper

the slope becomes. The exception to this trend is P1U4, which we will analyze in Sec. 4.3. Table 3 shows the ratio between the total initial magnetic energy and the energies at $T_A - T = 4$. For the non-rotating model, the remaining energy is only 1%, while P1U3 retains up to 60% (see top panel in Fig. 6). This suggests that rotation may suppress or at least delay the onset of the instability, leading to a slower decline in magnetic energy. These results are in agreement with previous findings (Braithwaite, J. 2007). However, we note that in P1U3 case, the most magnetically-stable case, the magnetic energy has not reached a steady equilibrium. Toward the end of our simulation ($T_A - T \sim 10$), the magnetic energy continues to decrease at the same rate. We cannot determine whether it will eventually settle or continue to decline. We speculate that because of the presence of numerical dissipation, the energy will keep falling. To assess the stability of these new magnetic field configurations (such as the one in the right panel of Fig. 5), higher-resolution and longer numerical simulations than those reported here are required to confirm this behavior. The energy values reported in Table 3 should be taken as estimates, as they may differ with resolution (see Appendix B).

The lower panel of Fig. 6 displays both the poloidal $E_{B_{\text{pol}}}$ and the toroidal $E_{B_{\text{tor}}}$ energies. As expected, the latest is initially null. Although all our configurations are initially uniformly rotating, the systems spontaneously developed differential rotation (see Fig. 4) which induces the growth of the toroidal energy. In the non-rotating case the $E_{B_{\text{tor}}}$ is $\sim 6\%$ of the initial magnetic energy, while in the highest rotating case the toroidal energy reaches a value of $\sim 14\%$ (see Table 3). For model P1U0, the growth of $E_{B_{\text{tor}}}$ coincides with the onset of the kink instability, i.e., the point where the total magnetic energy $E_{B_{\text{tot}}}$ changes slope. We note that the toroidal energy peaks at about 10% of $E_{B_{\text{tot}}}$, corresponding to the first appearance of a non-zero toroidal magnetic field component at $T_A - T \simeq 0.6$, as shown in Fig. 1. Afterward, it decays to roughly 6%. Before this epoch, the varicose instability mode appears earlier (see discussion above) at $T_A - T \sim -0.9$. This suggests that the varicose mode is likely associated with pinch-type instabilities related to the poloidal magnetic field configuration (Wright 1973).

On the other hand, the overall behavior of the rotating models is basically the same, though the evolution of $E_{B_{\text{tot}}}$ is more complex due to stellar rotation. Table 3 displays the

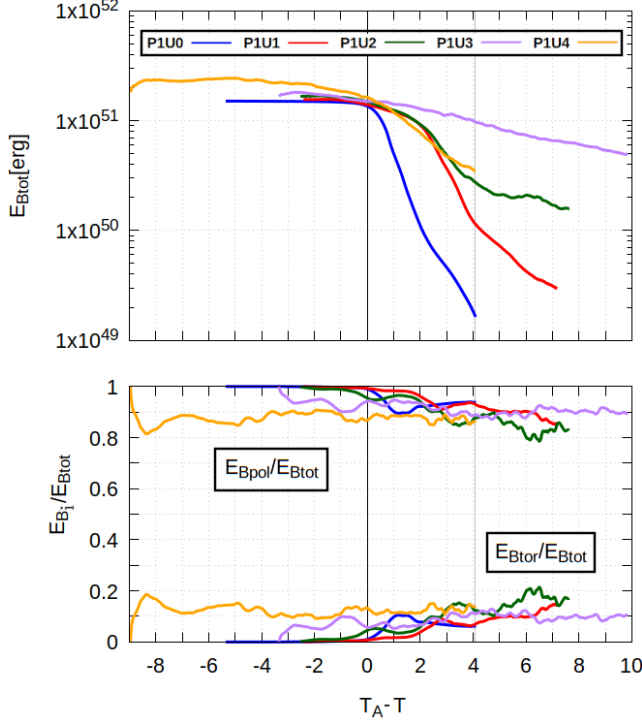


FIG. 6.— Total magnetic field energy $E_{B_{\text{tot}}}$ (up) and normalized toroidal magnetic field energy $E_{B_{\text{tor}}}$ and poloidal magnetic field energy $E_{B_{\text{pol}}}$ (down) vs. $T_A - T$. Here T is the time at which $E_{B_{\text{tot}}}$ has decreased by 10% of its initial value, which is our definition of the onset of the magnetic instabilities. The vertical gray line marks the termination of the P1U0 and P1U4 simulations. E_{B_i} denotes either $E_{B_{\text{tor}}}$ or $E_{B_{\text{pol}}}$ components.

toroidal magnetic energy at $T_A - T = 4$ for these models. Changes in the slope of the decay of $E_{B_{\text{tot}}}$ appear to coincide with the growth of the toroidal energy component in P1U1 and P1U2, suggesting a link between toroidal field growth and energy decay. However, this correlation is not observed in P1U3 and P1U4, and is less clear in P1U1 and P1U2 compared to the non-rotating case. It is likely that rotation suppresses, or at least delay, the onset of the kink instability. This implies that even when $E_{B_{\text{tor}}}$ increases, the total magnetic energy $E_{B_{\text{tot}}}$ may remain, at least initially, largely unaffected.

The spontaneous emergence of a toroidal magnetic field component from a purely poloidal configuration has also been reported in [Sur et al. \(2022\)](#) and [Cook et al. \(2023\)](#). [Sur et al. \(2022\)](#) found that the toroidal magnetic field energy decays to 1% of the total magnetic energy at ~ 6.5 Alfvén times, reaching only a quasi-stable equilibrium. In this configuration, most of the magnetic energy is converted into heat, while the rest is radiated away via a Poynting flux. On the other hand, the final outcome of the non-rotating model in ([Cook et al. 2023](#)) corresponds to a configuration with a toroidal magnetic field accounting 10% of the total magnetic energy after ~ 44 ms. Regarding the decay of magnetic energy, this effect has also been observed in numerical simulations (see e.g. [Braithwaite, J. \(2007\)](#); [Sur et al. \(2022\)](#)). [Braithwaite, J. \(2007\)](#) found that rotation slows the decay. In their case, the fastest rotating model (at the mass-shedding limit) retains $\lesssim 25\%$ of the initial energy. However, a comparison between their results and ours is difficult, as they do not report the simulation time in Alfvén units nor do they specify how the magnetic energy was calculated.

Finally, Fig. 7 displays the evolution of the internal energy, the kinetic energy, the pressure-contribution energy, and the

electromagnetic energy, all normalized to the total energy defined in Eq. (15), and plotted in units of the Alfvén crossing time. Over time, the kinetic (except for P1U0), pressure, and electromagnetic components decrease, while most of the total energy is gradually converted into internal energy. By the end of the simulations, internal energy is the only component that consistently increases across all models except for P1U0, the non-rotating case (see Table 1), where both the E_{kin} and the E_{prs} also increase. This is likely caused by the spontaneous emergence of the differential rotation (see Fig. 4). However, their final values remain roughly two orders of magnitude smaller than those in the rotating models, where E_{kin} and E_{prs} both decrease. We note that the total energy E_{tot} (not shown) is conserved to within 1% throughout the evolution.

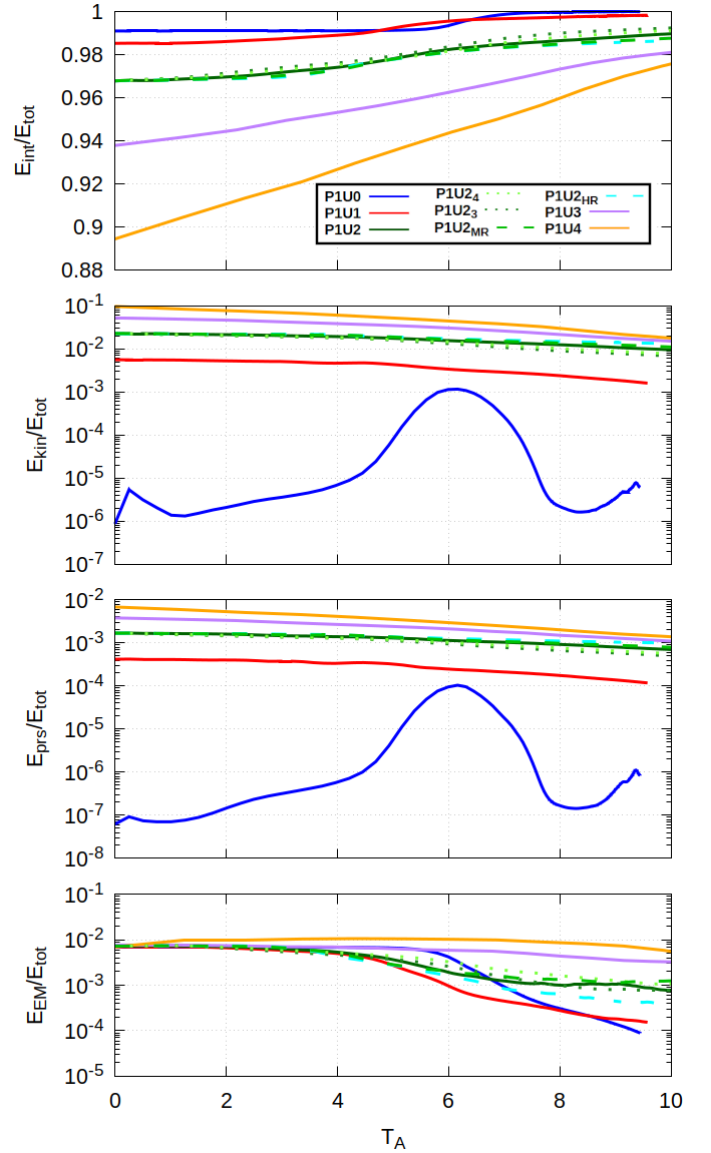


FIG. 7.— Evolution of the internal energy E_{int} (top panel), the kinetic E_{kin} energy (second panel), the pressure E_{prs} (third panel), and the electromagnetic energy E_{EM} (bottom panel) normalized by E_{tot} for all simulations of the models listed in Table 1, along with those models in appendices A and B.

4.3. Rotational timescale effects

Some instabilities can persist on a timescale of order $\tau_{\text{rot}} = \tau_A^2/T_r$ when the rotation period T_r is shorter than the Alfvén time τ_A . This was first pointed out by [Pitts & Tayler \(1985\)](#) and later discussed in more detail by [Spruit \(1999\)](#). The timescale τ_{rot} is equivalent to the τ_{MHD} of the Flowers-Ruderman mechanism ([Flowers & Ruderman 1977](#)), up to a factor of 2. To account for this timescale in our analysis, we define the Alfvén rotational crossing time as

$$T_{\text{rot}} = \int_0^t \frac{1}{\tau_A \sigma_{\text{rot}}} dt, \quad (26)$$

with $\sigma_{\text{rot}} = \tau_A/T_r$ when $\tau_A > T_r$, or $\sigma_{\text{rot}} = 1$ when $\tau_A \leq T_r$ ². We note that of the four rotating models, only PIU1 satisfies the condition $\tau_A \leq T_r$, and this occurs only at the beginning of the simulation before the Alfvén time increases.

Fig. 8 shows the evolution of magnetic energy versus T_{rot} for all our rotating models. Notice that, as our goal is to assess whether rotation delays the onset of instabilities, we do not shift the time by T . When expressed in units of T_{rot} , the differences in evolution times between the models become more pronounced. In particular, PIU4 approaches $T_{\text{rot}} = 1.5$, while PIU1 does not even reach $T_{\text{rot}} = 0.25$. This significant difference arises because the integral in Eq. (26) involves τ_A^2 , when $\tau_A > T$, unlike Eq. (18), and also due to the fact that the rotation period T_r varies between models.

For PIU1 and PIU2, it appears that the timescale required for instabilities to develop is shorter than τ_{rot} , suggesting that the system becomes unstable on an Alfvén timescale instead. In contrast, PIU3 and PIU4 seem to remain stable throughout several τ_A , raising the question of whether they can also survive over the longer τ_{rot} timescale. The energy decay observed in PIU3 may be attributed to numerical dissipation, while for PIU4, the decay may be also numerical before $T_{\text{rot}} \simeq 1$, after which the steeper drop indicates the onset of an instability associated with τ_{rot} .

Figure 1 shows that PIU4 develops a kink instability by $t = 12.5 T_A$. This suggests that rotation delays the onset of the instability but does not suppress it. We note that the resulting energy decline is more gradual than in the non-rotating model PIU0 (see Fig. 6). In units of τ_{rot} , the evolution of PIU3 terminates earlier than that of PIU4, which may explain why we do not yet observe a similarly steep decay. In Fig. 8, its energy decrease is more gradual, though it begins to steepen slightly after $T_{\text{rot}} = 0.5$. Longer simulations than those reported here are required to determine whether the system will exhibit a faster decay than PIU4 on this timescale.

4.4. Magnetic field misalignment

Although in all of our rotating configurations the NS initial dipole magnetic moment is aligned with its angular momentum (see Table 1), the system naturally evolves toward a configuration in which the dipole magnetic moment becomes misaligned with respect to the angular momentum. Fig. 9 displays the strength of the magnetic field at selected times along with the field lines configuration. Initially, the magnetic field strength is axisymmetric along the angular momentum direction and confined to $z \lesssim 2R_{\text{NS}}$ (first panel). As the field is

² In this work, we take the initial rotation periods in Table 1 for the Alfvén rotational crossing time. A more refined treatment would be to define an average rotation period at all times. However, we argue that the main behavior for T_{rot} is dominated by τ_A since, in Eq. (26), it is squared when $\tau_A > T_r$ (and the changes are more significant).

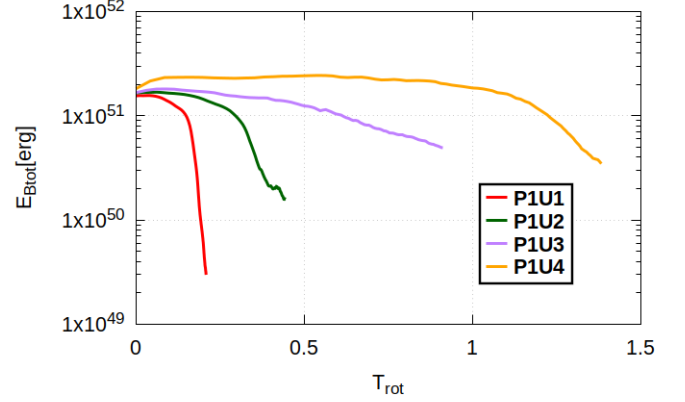


FIG. 8.— Total magnetic energy $E_{B_{\text{tot}}}$ vs. the Alfvén rotational crossing period T_{rot} .

frozen-in, by $t = 5$ ms (or $\sim 1.2T_A$), it has wound into a helical structure extending several NS radii along the angular momentum axis (second panel). However, for $t > 5$ ms (or $7T_A$), once instabilities set in, in particular, the kink instability, the dipole magnetic moment becomes misaligned and appears to precess around the angular momentum axis (third and fourth panels). The same behavior is observed in all other rotating cases. A similar effect has been reported, in the context of binary mergers, during the emergence of magnetically driven jets in ([Ruiz et al. 2021a,b](#)), where it has been attributed to the bouncing of magnetically dominated regions as they expand and have overcome the ram pressure of the infalling material.

To track the precession of the magnetic field, we compute the magnetic field average along the three Cartesian coordinates on a sphere S of coordinate radius 130 km and define the tilt angle as

$$\zeta = \arccos(B_{\text{avg}}^z/|B_{\text{avg}}|). \quad (27)$$

We use Eq. (27) to estimate the precession of the magnetic field. Top panel in Fig. 10 displays the precession of the magnetic field strength for all the rotating models. As expected, the tilt angle is initially zero, since all models begin with the magnetic dipole moment aligned along the direction of the angular momentum. By $t \lesssim 3T_A$, once some magnetic instabilities have set in, ζ begins to increase, and reaches a maximum peak after the onset of the kink instability. Near to the termination of the simulations, ζ seems to reach a quasi-steady state. The time average of ζ for each model is shown in Table 3. We note that the angle overall increases with angular velocity, although a small decrease is observed from PIU2 to PIU3. Longer and higher-resolution simulations are needed to determine its asymptotic value and investigate its long-term behavior. Note that the Eq. (27) definition is not gauge invariant. The tilt angle ζ depends on the radius of the spherical surface S over which the average is computed. This is illustrated in the lower panel of Fig. 10, which shows ζ as a function of the coordinate radius for model PIU4 at $\sim 8T_A$. Close to the star, the tilt angle is relatively small ($\lesssim 3^\circ$), but it increases with distance, reaching a maximum of approximately 28° , supporting the observation that tilt appears more pronounced farther from the star in Fig. 9. Beyond $r = 100$ km, however, ζ begins to decrease, falling to around 12° near the edge of the simulation domain, where the boundary and the square shape of the grid may influence this value.

5. DISCUSSION AND CONCLUSION

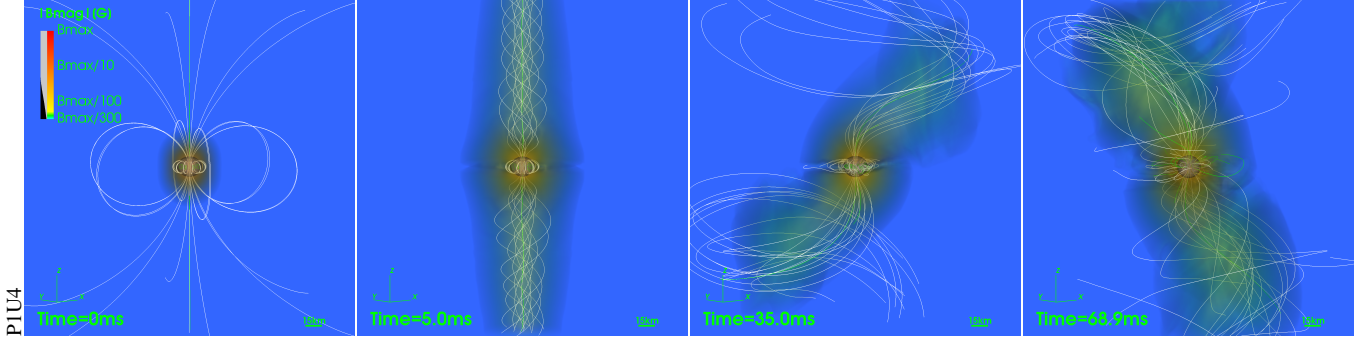


FIG. 9.— Strength of the magnetic field for P1U4 at selected times. White lines indicate the field lines. Notice that the colorbar limits are rescaled using B_{\max} at each time to account for changes in field strength. Similar behavior is observed across the other rotating cases.

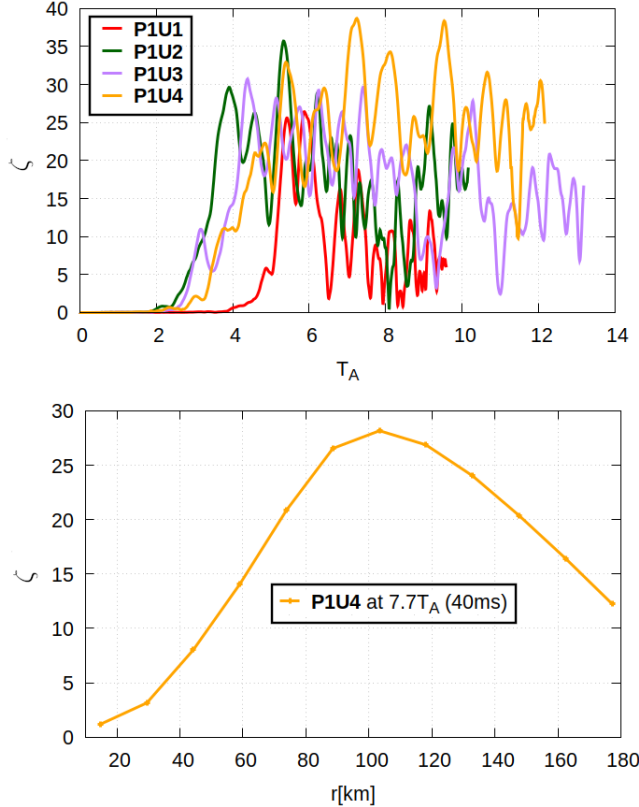


FIG. 10.— Top panel displays the evolution of the tilt angle ζ for all rotating models in Table 1 on a sphere of coordinate radius 130km. Bottom panel displays the tilt angle vs. different extraction radii for P1U4 at $7.7T_A$ (or 40ms).

The magnetic field stability in NSs remains an open question. Although simple models with purely toroidal or poloidal fields are unstable (Braithwaite & Nordlund 2006; Akgün et al. 2013), mixed configurations, especially axisymmetric ones with both components, may be stable in stars with stable internal layering (Braithwaite 2009b; Cioffi et al. 2009b). However, there is still no consensus on a universally stable configuration (Akgün et al. 2013).

As a step forward in understanding the emergence of magnetic instabilities that disrupt the stellar field configuration, we studied the impact of stellar rotation using full 3D general relativistic numerical simulations of uniformly rotating NS threaded by strong, poloidal, pulsar-like magnetic fields. The initial stellar configurations assume perfect conductivity and are stationary and axisymmetric. We explored a range of angular velocities, from non-rotating stars to those to half the

mass-shedding limit.

We found that all configurations spontaneously developed differential rotation, which in turn induces the formation of a toroidal magnetic field component that persists until the termination of our simulations. By examining the magnetic field structure, we observed that rotation can delay, or even suppress, the emergence of some magnetic instabilities. In the non-rotating case (P1U0), we found a clear relation between the magnetic field energy decay and the growth of the toroidal field, which is also related to the appearance of the kink instability. By contrast, in the rotating models this relation becomes less clear, with the decay of magnetic field energy appearing later. It is likely that, due to increasing rotation, the instability accompanied by the growth of the toroidal magnetic field is delayed.

Across all models, the total magnetic energy decays within a few Alfvén times, although rotation appears to slow this decay. We note that in all cases the magnetic energy is still decreasing by the termination of the simulations. However, as numerical dissipation is present in all our simulations, it remains difficult to assess whether the final magnetic field configurations are stable. We found that the faster the rotation, the slower is the decay of the magnetic field energy after the onset of the instability, except for the fastest rotating model. This indicates that there may be an optimal period value that makes the system retain most of its energy in the Alfvén crossing period timescale. This decrease in energy for the fastest rotating model is likely related to the instabilities of the timescale T_{rot} (for this timescale, P1U3 simulation is shorter than P1U4). Pitts & Tayler (1985); Spruit (1999) reported that rotation delays instabilities from the timescale τ_A to τ_{rot} when $T_r \ll \tau_A$. In our models, this inequality $T_r \ll \tau_A$ is poorly achieved by the fastest rotating model (and even less for the other models) at the beginning of our simulations. Nevertheless, we observe that the instabilities for the fastest model are more correlated to this timescale. It is likely that rotation can partially contain the instabilities by imposing an axisymmetric shape on the growing toroidal magnetic field, thereby preventing axisymmetry from breaking entirely. In this way, it may suppress the Parker instability and delay the kink instability, both of non-axisymmetric nature. Far from the NS, rotation has less effect, and therefore it fails to provide axisymmetry, observed with the magnetic field misalignment. On the other hand, as reported in (Braithwaite, J. 2007), some angle may be needed between a poloidal magnetic field and rotation to interact. In this work, misalignment appears naturally, allowing this interaction, although the end states of our simulations are a mixture of poloidal and toroidal magnetic field components so it raises the doubts about its importance.

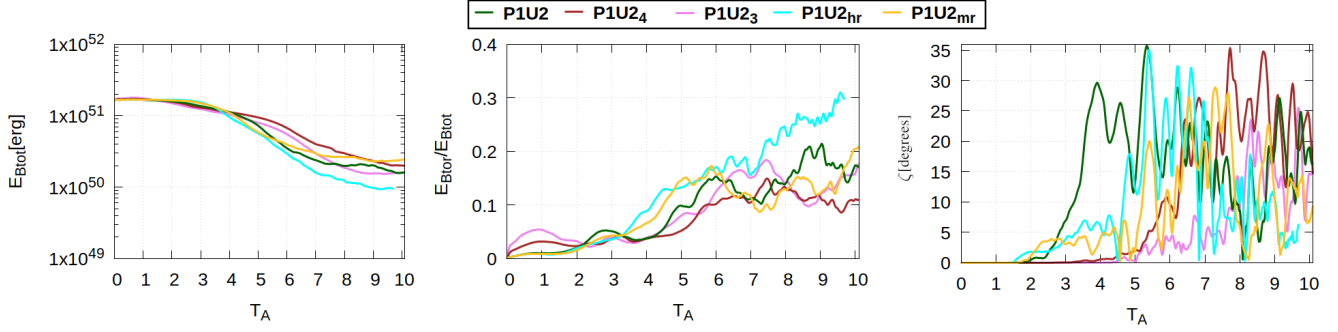


FIG. 11.— Evolution of the total magnetic energy (left), toroidal magnetic energy (middle), and the angle ζ between the magnetic field and the rotation axis (right) for P1U2, using three different atmosphere prescriptions, ranging from partial to full magnetic pressure dominance (Appendix A), and two higher resolutions (Appendix B).

It is worth noting that our simulations do not include a solid-crystalline crust, which could help prevent the dissipation of magnetic field energy and may play a crucial role in neutron star stability. We plan to explore this in future work.

This work has been supported by the Generalitat Valenciana (grants CIDEAGENT/2021/046, Prometeo CIPROM/2022/49 and CIGRIS/2022/126), and by the Spanish Agencia Estatal de Investigación (grants PID2021-125485NB-C21 funded by MCIN/AEI/10.13039/501100011033, PRE2019-087617, and ERDF A way of making Europe). Further support has been provided by the EU’s Horizon 2020 Research and Innovation (RISE) programme H2020-MSCA-RISE-2017 (FunFiCO-777740) and by the EU Staff Exchange (SE) programme

HORIZON-MSCA-2021-SE-01 (NewFunFiCO-101086251). We acknowledge computational resources and technical support of the Spanish Supercomputing Network through the use of MareNostrum at the Barcelona Supercomputing Center (AECT-2023-1-0006). A.K.L.Y. acknowledges the computational resources and technical support of the CUHK Central High-Performance Computing Cluster. A.K.L.Y. also acknowledges support from the Research Grants Council of Hong Kong (Project No. CUHK 14306419), the Croucher Innovation Award from the Croucher Foundation Hong Kong, and the Direct Grant for Research from the Research Committee of The Chinese University of Hong Kong. P.C.-K.C. gratefully acknowledges support from National Science Foundation (NSF) Grant PHY-2020275 (Network for Neutrinos, Nuclear Astrophysics, and Symmetries (N3AS)).

APPENDIX

IMPACT OF A VARIABLE MAGNETOSPHERE ON MAGNETIZED NEUTRON STAR EVOLUTION

We note that our density prescription for the MHD evolution of the magnetic field in the stellar exterior is only enforced initially. Subsequently, the density is evolved everywhere according to the ideal GRMHD equations, with a density floor imposed, as is standard in GRMHD simulations (Ruiz et al. 2018; Paschalidis et al. 2015). Empirically, we find that stable evolution requires heavier densities for faster-rotating NSs, likely because rotation induces stronger magnetic gradients. To explore the impact of the different density prescriptions, ranging from partial to full magnetic pressure dominance, we perform simulations of P1U2 with a magnetic-to-gas-pressure ratio $\beta^{-1} = 10^{-3}, 10^{-4}, 10^{-6}$, denoted as P1U2₃, P1U2₄ and P1U2, respectively.

The left panel in Fig. 7 displays the evolution of different energies (see Eqs. (7)-(10)) for the above cases. We note that, regardless of the initial density prescription, all energy components evolve following the same trend with no significant changes between them. Fig. 11 shows the evolution of the total magnetic energy E_{Btot} . We observe that changes induced by the different atmosphere prescriptions are $\lesssim 3\%$ (see Table 4), compared to those with different angular velocities, where changes range from $\sim 6\%$ to $\sim 58\%$ (see Table 3).

As noted earlier, the stars spontaneously develop differential rotation, which leads to the emergence of a strong toroidal magnetic field component that persists until the end of our simulations. As shown in the middle panel of Fig. 7, different atmospheres affect the magnitude of the toroidal magnetic field component. Near the end of our simulations, we observe variations of about $\sim 8\%$ in the toroidal field strength across the evolved models (see Table 4). However, by $t \sim 10T_A$ the system has not yet reached a steady state, and longer simulations are therefore required to fully assess the impact of the atmosphere on the growth of the toroidal magnetic field component.

Fig. 12 shows the angular velocity profiles for these three cases. During the early evolution, we observe that models with a heavier atmosphere exhibit sharper differential rotation in the inner region of the star. However, after ~ 10 ms, the stars roughly recover a uniform rotation of ~ 1.25 kHz for P1U2, and slightly lower values (~ 1.1 kHz) for the other cases.

Finally, it is worth noting that the tilt angle, shown in Fig. 11, is roughly the same for cases with $\beta = 10^{-4}$ and 10^{-6} , but changes significantly for the $\beta = 10^{-3}$ case (see Table 4). This is likely due to the larger ram pressure that the field lines must overcome. Longer numerical simulations are needed to probe the impact of heavier atmospheres in the tilt angle.

INFLUENCE OF RESOLUTION ON MAGNETIC EVOLUTION

To assess the dependence of our results on the numerical resolution, we consider two additional P1U2 cases using higher resolutions: i) P1U2_{MR}, where we employ a resolution of $N_x \times N_y \times N_z = 96^3$; and ii) P1U2_{HR}, with $N_x \times N_y \times N_z = 128^3$. Both simulations use five AMR levels, differing in size and resolution by a factor of two, i.e. we are employing one additional refinement level compared to our canonical cases. The finest grid size at the center of the star is $\Delta x = \Delta y = \Delta z \approx 230$ m for

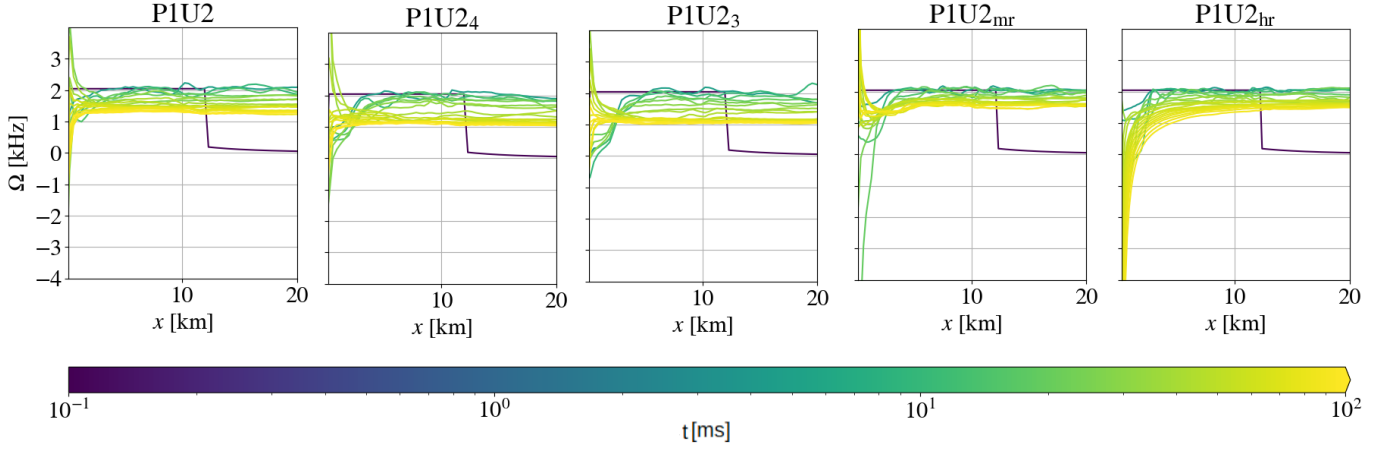


FIG. 12.— Angular velocity profiles along the coordinate x -axis for P1U2 using three different atmosphere prescriptions, ranging from partial to full magnetic pressure dominance (Appendix A), and two higher resolutions (Appendix B).

TABLE 4

COMPARISON OF THE EVOLUTION OF P1U2 EVOLVED USING DIFFERENT ATMOSPHERE PRESCRIPTION AND HIGHER RESOLUTIONS. WE LIST THE FRACTION OF THE INITIAL TOTAL MAGNETIC ENERGY $E_{B_{\text{tot}}}$ REMAINING AROUND THE TERMINATION OF OUR SIMULATIONS ($\sim 9.5T_A$), THE TOROIDAL-TO-TOTAL MAGNETIC ENERGY RATIO AT THAT POINT, AND THE MAGNETIC FIELD TILT ANGLE WITH RESPECT TO THE ROTATION AXIS FOR ALL NS MODELS.

MODEL	$E_{B_{\text{tot}}}/E_{B_{\text{tot}0}}$	$E_{B_{\text{tor}}}/E_{B_{\text{tot}}}$	$\zeta_{\text{avg}} [^\circ]$
P1U2	10.4%	16.9%	14.6
P1U2 ₄	12.6%	9.3%	14.6
P1U2 ₃	9.3%	14.2%	7.8
P1U2 _{MR}	13.6%	11.1%	10.4
P1U2 _{HR}	5.8%	29.6%	10.1

P1U2_{MR} and $\Delta x = \Delta y = \Delta z \approx 173$ m for P1U2_{HR}. All other aspects of the two simulations are identical to those of the canonical P1U2 case. In particular, we set $\beta^{-1} = 10^{-6}$ in these two cases.

Fig. 7 shows the evolution of different energies (see Eqs. (7)–(10)). In general, we find that numerical resolution has only a minor impact on all energies, with variations smaller than 2%, except E_{EM} . Although the overall trend in E_{EM} is consistent across all cases, it exhibits a more pronounced decay in P1U2_{HR} than in P1U2. By contrast, the electromagnetic energy in P1U2_{MR} and P1U2 remains roughly the same (see bottom panel of Fig. 7). We also note that since this energy is roughly an order of magnitude smaller than the other energies, its behavior only marginally affects the internal energy.

The left panel of Fig. 11 shows the evolution of the total magnetic energy $E_{B_{\text{tot}}}$. During the first $t \sim 4T_A$, numerical resolution has a minor impact on its evolution. However, after the onset of magnetic instabilities, a stronger toroidal magnetic field component develops in the highest-resolution case (see middle panel in Fig. 11). As shown in Fig. 12, differential rotation is also more pronounced in this case, leading to a more rapid decay of the total magnetic energy than in the other cases (see Table 4). In particular, the energy decays by a factor of ~ 1.8 in P1U2_{HR} compared to P1U2. By contrast, in P1U2_{MR} the total magnetic energy near the end of the simulations is about 1.3 times larger than in P1U2. Similar behavior has been reported in (Sur et al. 2022).

Finally, the tilt angle ζ , shown in the right panel of Fig. 11, is slightly smaller in the high-resolution cases than in the canonical P1U2 (see Table 4). This suggests that numerical viscosity may play a significant role in the precession of the magnetic field lines, indicating that higher-resolution simulations are required to assess its impact on the tilt angle.

REFERENCES

- Acheson, D. J., & Gibbons, M. P. 1978, *Philosophical Transactions of the Royal Society of London Series A*, 289, 459
- Aguilera-Mir, R., Palenzuela, C., Carrasco, F., Rosswog, S., & Viganò, D. 2024, *Phys. Rev. D*, 110, 083014, 2407.20335
- Akgün, T., Reisenegger, A., Mastrano, A., & Marchant, P. 2013, *MNRAS*, 433, 2445, 1302.0273
- Ascenzi, S., Graber, V., & Rea, N. 2024, *Astropart. Phys.*, 158, 102935, 2401.14930
- Bamber, J., Tsokaros, A., Ruiz, M., & Shapiro, S. L. 2025, *Phys. Rev. D*, 111, 044038, 2411.00943
- Baumgarte, T. W., & Shapiro, S. L. 2010, *Numerical Relativity: Solving Einstein's Equations on the Computer*
- Begelman, M. C. 1998, *Astrophys. J.*, 493, 291, astro-ph/9708142
- Bethe, H. A., & Brown, G. E. 1995, *ApJ*, 445, L129
- Bhattacharya, D., & Srinivasan, G. 1991, *The Evolution of Neutron Star Magnetic Fields*, ed. J. Ventura & D. Pines (Dordrecht: Springer Netherlands), 219–233
- Bonazzola, S., & Gourgoulhon, E. 1996, *Astron. Astrophys.*, 312, 675, astro-ph/9602107
- Braithwaite, J. 2009a, *Monthly Notices of the Royal Astronomical Society*, 397, 763, <https://academic.oup.com/mnras/article-pdf/397/2/763/2932157/mnras0397-0763.pdf>
- . 2009b, *Mon. Not. Roy. Astron. Soc.*, 397, 763, 0810.1049
- Braithwaite, J., & Nordlund, A. 2005, *Astronomy and Astrophysics*, 450
- . 2006, *Astron. Astrophys.*, 450, 1077, astro-ph/0510316
- Braithwaite, J., & Spruit, H. C. 2004, *Nature*, 431, 819, astro-ph/0502043
- . 2006a, *Astron. Astrophys.*, 450, 1097, astro-ph/0510287
- . 2006b, *Astronomy & Astrophysics*, 450, 1097–1106
- Braithwaite, J. 2007, *A&A*, 469, 275

- Brandenburg, A., & Subramanian, K. 2005, *Phys. Rep.*, 417, 1, astro-ph/0405052
- Bucciantini, N., & Del Zanna, L. 2011, *Astronomy & Astrophysics*, 528, A101
- Burrows, A., Dessart, L., Livne, E., Ott, C. D., & Murphy, J. 2007, *Astrophys. J.*, 664, 416, astro-ph/0702539
- Camilo, F., Thorsett, S. E., & Kulkarni, S. R. 1994, *ApJ*, 421, L15
- Cheong, P. C.-K., Lam, A. T.-L., Ng, H. H.-Y., & Li, T. G. F. 2021a, *Mon. Not. Roy. Astron. Soc.*, 508, 2279, 2012.07322
- . 2021b, *Monthly Notices of the Royal Astronomical Society*, 508, 2279–2301
- Cheong, P. C.-K., Lin, L.-M., & Li, T. G. F. 2020, *Classical and Quantum Gravity*, 37, 145015
- Cheong, P. C.-K., Ng, H. H.-Y., Lam, A. T.-L., & Li, T. G. F. 2023, *The Astrophysical Journal Supplement Series*, 267, 38
- Cheong, P. C.-K., Pong, D. Y. T., Yip, A. K. L., & Li, T. G. F. 2022, *The Astrophysical Journal Supplement Series*, 261, 22
- Cheong, P. C.-K., Tsokaros, A., Ruiz, M., Venturi, F., Chan, J. C. L., Yip, A. K. L., & Uryū, K. 2025, *Phys. Rev. D*, 111, 063030, 2409.10508
- Cioffi, R., Ferrari, V., & Gualtieri, L. 2010, *Mon. Not. Roy. Astron. Soc.*, 406, 2540, 1003.2148
- Cioffi, R., Ferrari, V., Gualtieri, L., & Pons, J. A. 2009a, *Mon. Not. Roy. Astron. Soc.*, 397, 913, 0903.0556
- . 2009b, *Mon. Not. Roy. Astron. Soc.*, 397, 913, 0903.0556
- Colella, P., & Woodward, P. R. 1984, *Journal of Computational Physics*, 54, 174
- Cook, W., Daszuta, B., Fields, J., Hammond, P., Albanesi, S., Zappa, F., Bernuzzi, S., & Radice, D. 2023, *GR-Athena++: General-relativistic magnetohydrodynamics simulations of neutron star spacetimes*, 2311.04989
- Cordero-Carrión, I., Cerdá-Durán, P., Dimmelfeier, H., Jaramillo, J. L., Novak, J., & Gourgoulhon, E. 2009, *Physical Review D*, 79
- Cutler, C. 2002, *Phys. Rev. D*, 66, 084025, gr-qc/0206051
- Duncan, R. C., & Thompson, C. 1992, *ApJ*, 392, L9
- Evans, C. R., & Hawley, J. F. 1988, *ApJ*, 332, 659
- Ferrario, L., & Wickramasinghe, D. 2006, *Mon. Not. Roy. Astron. Soc.*, 367, 1323, astro-ph/0601258
- Flowers, E., & Ruderman, M. A. 1977, *ApJ*, 215, 302
- Gabler, M., Cerdá-Durán, P., Font, J. A., Müller, E., & Stergioulas, N. 2011, *Mon. Not. Roy. Astron. Soc.*, 410, 37, 1007.0856
- Gabler, M., Cerdá-Durán, P., Font, J. A., Müller, E., & Stergioulas, N. 2013, *MNRAS*, 430, 1811, 1208.6443
- Geppert, U., & Rheinhardt, M. 2006, *Astronomy and Astrophysics*, 456, 639
- Glampedakis, K., & Lasky, P. D. 2015, *MNRAS*, 450, 1638, 1501.05473
- Goldreich, P., & Julian, W. H. 1969, *ApJ*, 157, 869
- Harten, A., Lax, P., & Leer, B. 1983, *SIAM Review*, 25, 35, <https://doi.org/10.1137/1025002>
- Keppens, R., Popescu Braileanu, B., Zhou, Y., Ruan, W., Xia, C., Guo, Y., Claes, N., & Bacchini, F. 2023, *A&A*, 673, A66, 2303.03026
- Keppens, R., Teunissen, J., Xia, C., & Porth, O. 2020, *MPI-AMRVAC: a parallel, grid-adaptive PDE toolkit*, 2004.03275
- Kiuchi, K., Reboul-Salze, A., Shibata, M., & Sekiguchi, Y. 2024, *Nature Astron.*, 8, 298, 2306.15721
- Kiuchi, K., Shibata, M., & Yoshida, S. 2008a, *Phys. Rev. D*, 78, 024029, 0805.2712
- . 2008b, *Physical Review D*, 78
- Kiuchi, K., Yoshida, S., & Shibata, M. 2011, *A&A*, 532, A30
- Konar, S., & Bhattacharya, D. 1997, *MNRAS*, 284, 311
- Kruskal, M., & Schwarzschild, M. 1954, *Proceedings of the Royal Society of London Series A*, 223, 348
- Lander, S. K. 2013, *Phys. Rev. Lett.*, 110, 071101, 1211.3912
- Lander, S. K., & Jones, D. I. 2009, *MNRAS*, 395, 2162, 0903.0827
- . 2011, *MNRAS*, 412, 1730, 1010.0614
- Lattimer, J. M., & Prakash, M. 2001, *Astrophys. J.*, 550, 426, astro-ph/0002232
- Markey, P., & Tayler, R. J. 1973, *MNRAS*, 163, 77
- Mereghetti, S. 2008, *A&A Rev.*, 15, 225, 0804.0250
- Parker, E. N. 1966, *ApJ*, 145, 811
- Paschalidis, V., Ruiz, M., & Shapiro, S. L. 2015, *Astrophys. J. Lett.*, 806, L14, 1410.7392
- Pili, A. G., Bucciantini, N., & Del Zanna, L. 2014, *Monthly Notices of the Royal Astronomical Society*, 439, 3541, <https://academic.oup.com/mnras/article-pdf/439/4/3541/3981452/stu215.pdf>
- . 2015, *Monthly Notices of the Royal Astronomical Society*, 447, 2821, <https://academic.oup.com/mnras/article-pdf/447/3/2821/9387552/stu2628.pdf>
- . 2017, *Monthly Notices of the Royal Astronomical Society*, 470, 2469, <https://academic.oup.com/mnras/article-pdf/470/2/2469/18245433/stx1176.pdf>
- Pitts, E., & Tayler, R. J. 1985, *Monthly Notices of the Royal Astronomical Society*, 216, 139, <https://academic.oup.com/mnras/article-pdf/216/2/139/3499775/mnras216-0139.pdf>
- Prendergast, K. H. 1956, *ApJ*, 123, 498
- Reisenegger, A. 2003, in *International Workshop on Strong Magnetic Fields and Neutron Star*, 33–49, astro-ph/0307133
- Reisenegger, A. 2013, *Magnetic fields of neutron stars*, 1305.2542
- Rembiasz, T., Guilet, J., Obergaulinger, M., Cerdá-Durán, P., Aloy, M. A., & Müller, E. 2016, *MNRAS*, 460, 3316, 1603.00466
- Ruiz, M., Shapiro, S. L., & Tsokaros, A. 2018, *Phys. Rev. D*, 98, 123017, 1810.08618
- . 2021a, *Front. Astron. Space Sci.*, 8, 39, 2102.03366
- Ruiz, M., Tsokaros, A., & Shapiro, S. L. 2021b, *Phys. Rev. D*, 104, 124049, 2110.11968
- Shu, C.-W., & Osher, S. 1988, *Journal of Computational Physics*, 77, 439
- Sotani, H., Kokkotas, K. D., & Stergioulas, N. 2007, *Mon. Not. Roy. Astron. Soc.*, 375, 261, astro-ph/0608626
- Spruit, H. C. 1999, *A&A*, 349, 189, astro-ph/9907138
- Spruit, H. C. 2008, *AIP Conf. Proc.*, 983, 391, 0711.3650
- Sur, A., Cook, W., Radice, D., Haskell, B., & Bernuzzi, S. 2022, *Monthly Notices of the Royal Astronomical Society*, 511, 3983–3993
- Tayler, R. J. 1973, *MNRAS*, 161, 365
- Taylor, J. B. 1986, *Reviews of Modern Physics*, 58, 741
- Thompson, C., & Duncan, R. C. 1993, *ApJ*, 408, 194
- . 1995, *MNRAS*, 275, 255
- . 1996, *ApJ*, 473, 322
- Tsokaros, A., Ruiz, M., Shapiro, S. L., & Uryū, K. 2022, *Physical Review Letters*, 128
- Viganò, D., García-García, A., Pons, J. A., Dehman, C., & Graber, V. 2021, *Comput. Phys. Commun.*, 265, 108001, 2104.08001
- Wasserman, I. 2003, *MNRAS*, 341, 1020, astro-ph/0208378
- Woosley, S. E., Heger, A., & Weaver, T. A. 2002, *Reviews of Modern Physics*, 74, 1015
- Wright, G. A. E. 1973, *Monthly Notices of the Royal Astronomical Society*, 162, 339, <https://academic.oup.com/mnras/article-pdf/162/4/339/8073447/mnras162-0339.pdf>
- Wright, G. A. E. 1973, *MNRAS*, 162, 339
- Xia, C., Teunissen, J., Mellah, I. E., Chané, E., & Keppens, R. 2018, *The Astrophysical Journal Supplement Series*, 234, 30